Applied Surface Science 347 (2015) 777–783

Contents lists available at ScienceDirect

Applied Surface Science

journal homepage: www.elsevier.com/locate/apsusc

Structural and XPS studies of PSi/TiO_2 nanocomposites prepared by ALD and Ag-assisted chemical etching

Igor Iatsunskyi[a,*], Mateusz Kempiński[a,b], Grzegorz Nowaczyk[a], Mariusz Jancelewicz[a], Mykola Pavlenko[c], Karol Załęski[a], Stefan Jurga[a,d]

[a] NanoBioMedical Centre, Adam Mickiewicz University, 85 Umultowska Str., 61-614 Poznan, Poland
[b] Faculty of Physics, Adam Mickiewicz University, Umultowska 85, 61-614, Poland
[c] Department of Experimental Physics, Odessa National I.I. Mechnikov University, 42, Pastera Str., 65023 Odessa, Ukraine
[d] Department of Macromolecular Physics, Adam Mickiewicz University, Umultowska 85, 61-614 Poznan, Poland

ARTICLE INFO

Article history:
Received 9 March 2015
Received in revised form 23 April 2015
Accepted 23 April 2015
Available online 2 May 2015

Keywords:
Atomic layer deposition
XPS
Porous silicon
Dioxide titanium
Nanocomposites

ABSTRACT

PSi/TiO_2 nanocomposites fabricated by atomic layer deposition (ALD) and metal-assisted chemical etching (MACE) were investigated. The morphology and phase structure of PSi/TiO_2 nanocomposites were studied by means of scanning electron microscopy (SEM), transmission electron microscopy (TEM) with an energy dispersive X-ray spectroscopy (EDX) and Raman spectroscopy. The mean size of TiO_2 nanocrystals was determined by TEM and Raman spectroscopy. X-ray photoelectron spectroscopy (XPS) was used to analyze the chemical elemental composition by observing the behavior of the Ti 2p, O 1s and Si 2p lines. TEM, Raman spectroscopy and XPS binding energy analysis confirmed the formation of TiO_2 anatase phase inside the PSi matrix. The XPS valence band analysis was performed in order to investigate the modification of PSi/TiO_2 nanocomposites electronic structure. Surface defects states of Ti^{3+} at PSi/TiO_2 nanocomposites were identified by analyzing of XPS valence band spectra.

1. Introduction

Nanocomposites based on silicon nanostructures and metal oxides (MOx) have drawn increased attention in different applications, such as in sensors and biosensors [1–5], catalysis [6–8], photovoltaics [9,10], electronics [11,12] and optics [13–15]. Among different metal oxides, TiO_2 is one of the most important materials. This material is used in many applications: photocatalysts [7,8], solar cell electrodes [16,17], and modern electronic optical devices [18]. Recent interest has been paid by researchers to the nano-scale TiO_2, which has highly active surface area and demonstrates new properties, induced by quantum-size effects [19,20]. On the other hand, porous silicon (PSi) structures have unique physical properties such as the biocompatibility, the large surface area, flexibility in tuning the structural parameters and finally its compatibility with the modern IC (integrated circuit) industry. Nanocomposites based on PSi and TiO_2 benefit from the unique properties of both components for development and improvement of various optical and electronic devices. PSi/TiO_2 nanocomposites also show improved photocatalytic efficiency due to the enhanced separation of excited electrons and holes. In this regard, the structure and electronic properties study of PSi/TiO_2 nanocomposites have gained increasing attention in the last years.

Here we report the first, to our knowledge, study of the structural and electronic properties of PSi/TiO_2 nanocomposites obtained by atomic layer deposition (ALD) and metal-assisted chemical etching (MACE). Titanium dioxide nanocrystals were introduced inside the PSi matrix to fabricate PSi/TiO_2 nanocomposites. For this purpose we used ALD. ALD is a deposition process for highly uniform and conformal thin films. Due to chemical reactions in the ALD process, very conformal and thickness controlled films can be grown over large areas even inside the PSi [12,21]. The surface morphology and phase structure of PSi/TiO_2 nanocomposites were detected by scanning electron microscopy (SEM), transmission electron microscopy (TEM) with an EDX analyzer, Raman spectroscopy and X-ray photoelectron spectroscopy (XPS). The results obtained are very promising for the improved use of PSi/TiO_2 nanocomposites in photocatalysts, photovoltaic and sensor application where it is important to tune their physical properties by the morphology of PSi/TiO_2.

* Corresponding author. Tel.: +48 731308173.
E-mail address: yatsunskiy@gmail.com (I. Iatsunskyi).

http://dx.doi.org/10.1016/j.apsusc.2015.04.172
0169-4332/

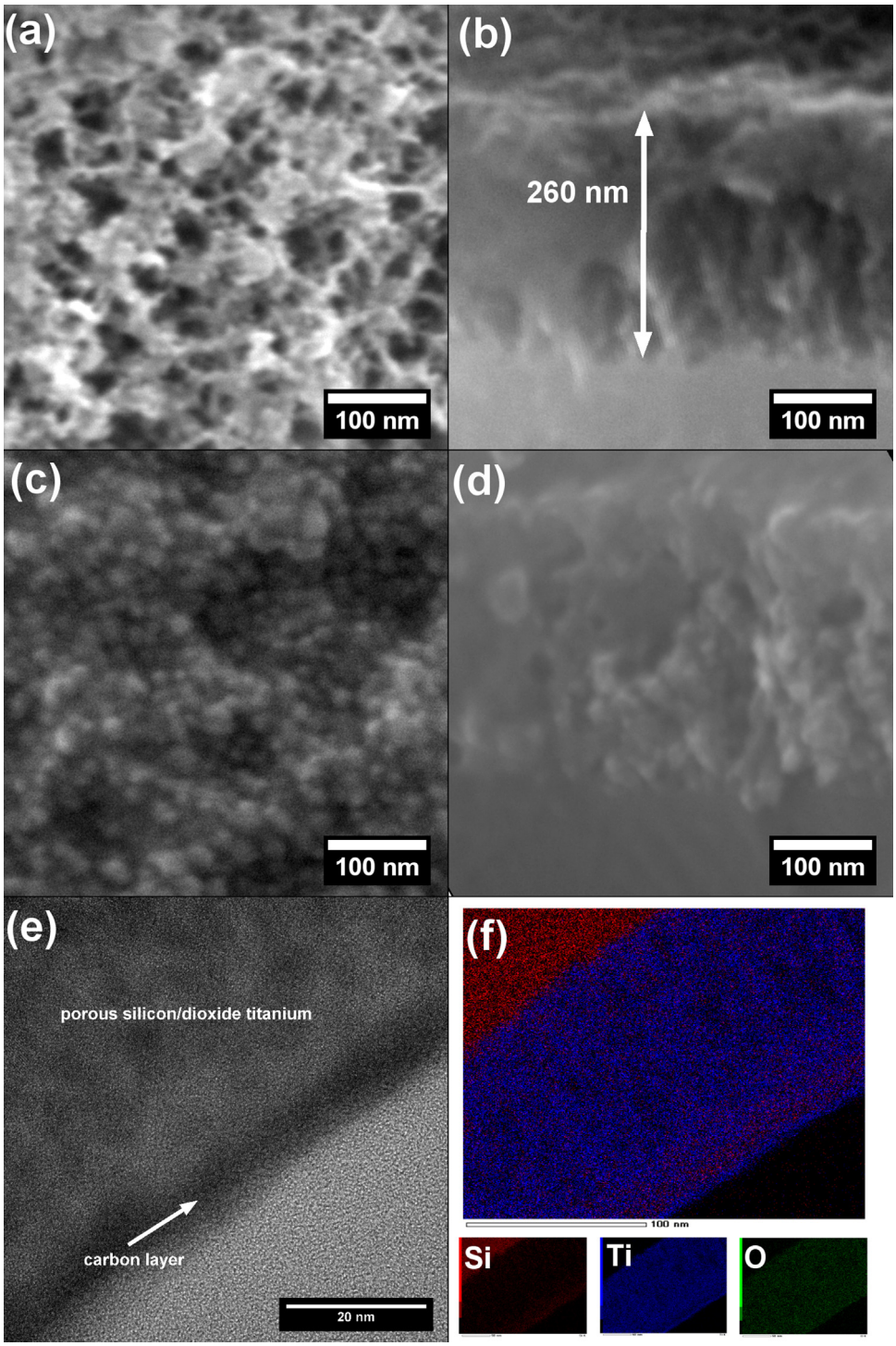

Fig. 1. (a) Plane and (b) cross-sectional view of as-prepared PSi, (c) plane and (d) cross-sectional view of the PSi/TiO_2 nanocomposite (150 ALD cycles), (e) TEM cross-sectional image and (f) cross-sectional EDX elemental mapping of the PSi/TiO_2 nanocomposite (150 ALD cycles).

2. Experimental details

2.1. Preparation of PSi/TiO_2 nanocomposites

In this study, PSi/TiO_2 nanocomposites were obtained by ALD and MACE [22]. Prior to the ALD process, PSi samples were fabricated from (1 0 0) oriented and highly doped p-type Si (B-doped, $\rho < 0.005\ \Omega$ cm). The silver particles, which act as catalysts to assist the etching of silicon, were deposited on Si samples by immersion in 0.2 M HF and 10^{-3} M $AgNO_3$ metallization aqueous solutions. The time of immersion was 60 s. Then, the samples were etched in aqueous solutions containing HF (40%), H_2O_2 (30%), and ultrapure H_2O at ratio concentration $H_2O_2/H_2O/HF = 80/80/20$ for 60 min. After MACE and removing the silver particles using a HNO_3 solution for 60 min, TiO_2 was deposited at 300 °C using ALD reactor (Picosun) with precursors of titanium(IV) chloride ($TiCl_4$) and water (H_2O). The $TiCl_4$ and H_2O were evaporated at 20 °C. In this study, the standard cycle consisted of 0.1 s exposure to $TiCl_4$, 3 s N_2 purge, 0.1 s exposure to water and 4 s N_2 purge. The total flow rate of the N_2 was 150 sccm. The growth rate was typically 0.5 Å/cycle for TiO_2

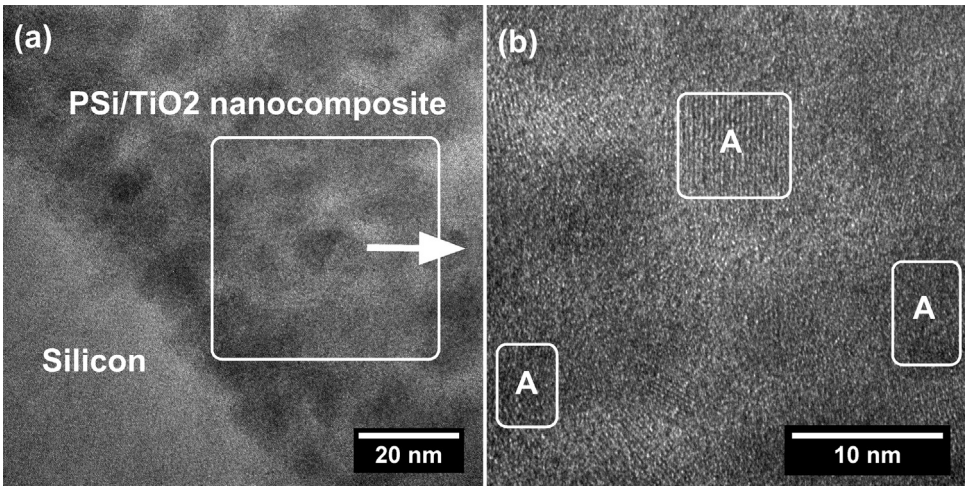

Fig. 2. Cross-sectional HRTEM images of the PSi/TiO_2 nanocomposite after 200 ALD cycles. (a) View of the PSi/TiO_2–Si interface. (b) View of the highlighted white square; the nanocrystallites denoted by 'A' can be identified as anatase TiO_2 (1 0 1) type planes.

on the planar silicon surface. Different number of ALD cycles (100, 150 and 200) was applied to prepare PSi/TiO_2 nanocomposites.

2.2. Material characterization

The obtained PSi/TiO_2 nanocomposites were characterized by various techniques. The morphology of the nanocomposite surface was investigated by scanning electron microscopy (JEOL, JSM-7001F) with an EDX analyzer. Transmission electron microscopy (TEM) images were obtained with a JEOL ARM 200F high-resolution (HR) TEM (200 kV) with an EDX analyzer. The cross-sections and lamellas for TEM investigations were prepared by Focused Ion Beam (JEOL, JIB-4000). Raman scattering measurements were performed using a Renishaw micro-Raman spectrometer equipped with a confocal microscope (Leica). The structure and the chemical state of PSi/TiO_2 nanocomposites were analyzed by means of the X-ray photoelectron spectroscopy (XPS) technique mounted within the Omicron Nanotechnology multiprobe UHV system, using a monochromatized Al-Kα X-ray as the excitation source and choosing C 1s (284.6 eV) as the reference line. XPS was conducted under ultrahigh vacuum (10^{-10} mbar). CasaXPS software was used to analyze the XPS data.

3. Results and discussion

3.1. Electron microscopy

Fig. 1 shows the SEM and TEM images of PSi and PSi/TiO_2 nanocomposites obtained by ALD and MACE. The PSi layer consists of large number of small pores. The average pore size is about 15–30 nm (Fig. 1a). The cross-sectional SEM view of the PSi shows the presence of pores propagating into the bulk from the surface in a perpendicular manner (Fig. 1b). The thickness of the PSi layer is approximately 260 nm. After ALD process, the PSi layer consists of spherical grains uniformly distributed over the surface (Fig. 1c). Depending on the number of ALD cycles, an average grain size ranged from 20 to 40 nm. Cross-sectional SEM and TEM images show that the ALD TiO_2 infiltrates and coats the pores conformally (Fig. 1d and e). The EDX mapping image showing the distribution of Si, Ti and O atoms is presented in Fig. 1f. It confirms that the Ti and O atoms penetrate quite uniformly into the PSi matrix. During the ALD process molecules of precursors penetrate into the pore forming the layer or other structures of TiO_2 inside the PSi matrix. Wang et al. reported that the diffusion of the precursor molecules into the porous media, having approximate pore size about 9 nm or less, is generally difficult and limited [23]. In our case, the average pore size is bigger than 9 nm to allow the precursor molecules to penetrate freely into the pore.

TiO_2 nanocrystallites were identified in the PSi matrix by applying high resolution cross-sectional TEM (Fig. 2). Fig. 2a shows the PSi/TiO_2–Si interface. The interface, parts of the pore walls and TiO_2 crystallites can be distinguished. The nanocrystallites denoted by 'A' in Fig. 2b can be associated with anatase (1 0 1) type crystalline planes with $d = 3.5$ Å. The diameters of the nanocrystallites are 5–8 nm.

3.2. Raman spectroscopy

In order to confirm the composition of PSi/TiO_2, Raman spectroscopy has been used (Fig. 3). We have found that Raman spectroscopy is more sensitive to the surface region of TiO_2 than XRD. The peak at 520 cm^{-1}, which is characteristic of crystalline silicon, arises from the scattering of incident light by the first order longitudinal and transversal optical phonon (LTO) in the diamond structures of PSi [24,25]. Raman spectra of the as-prepared PSi/TiO_2 showed no significant peaks of TiO_2 in the background of the strong spectrum of the PSi, indicating the small amount and/or the

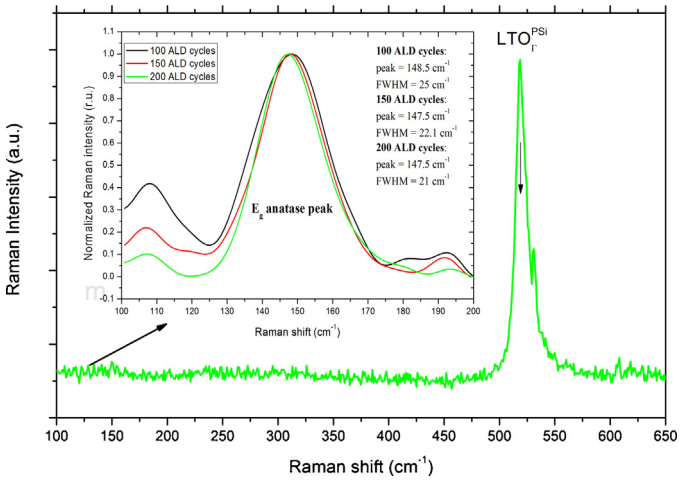

Fig. 3. Raman spectrum of the PSi/TiO_2 after 200 ALD cycles (laser power – 1 mW). (inset) Raman spectra of PSi/TiO_2 nanocomposites (laser power – 10 mW).

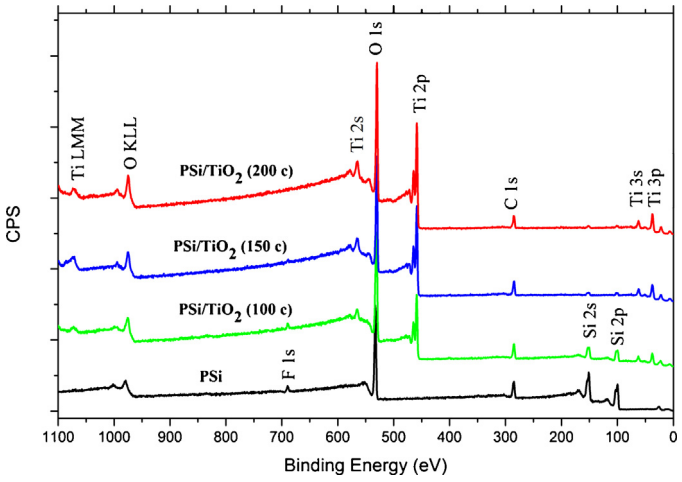

Fig. 4. XPS survey spectra of the PSi (black curve) and PSi-TiO_2 nanocomposites (100 ALD cycles – green curve, 150 ALD cycles – blue curve and 200 ALD cycles – red curve). The main core levels are labeled. The data are normalized to each O1s peak maximum and separated vertically. (For interpretation of the references to color in this figure legend, the reader is referred to the web version of this article.)

amorphous phase of TiO_2. However, increasing the power of the laser beam allowed us to observe the Raman peak at about 147 cm^{-1}, corresponding to the anatase phase of TiO_2 (inset of Fig. 3). It is typical of the anatase TiO_2 phase, but the peak is broader and shifted with respect to the bulk anatase (peak position is 144 cm^{-1} and a full width at half maximum – FWHM, is 7 cm^{-1}) [26,27]. With increasing the number of ALD cycles, the Raman peak shifts toward low wavenumbers and the FWHM becomes smaller. This shift could be explained by two different mechanisms: a stress effect of the PSi matrix on the TiO_2 crystallites and quantum confinement effects in anatase nanocrystals [27–29]. More likely, both mechanisms affect the shift and the broadening of the Raman peak.

Comparing these results with TEM findings we can conclude that very small amount of anatase nanocrystals have formed for as-prepared PSi/TiO_2 structures. In order to increase the concentration of anatase nanocrystals inside the PSi matrix, an additional thermal treatment should be performed.

3.3. XPS analysis

3.3.1. Survey spectra

In order to determine the chemical composition of the PSi and PSi/TiO_2 nanocomposites, we used XPS analysis. Fig. 4 shows the XPS survey spectra of the PSi and PSi/TiO_2 nanocomposites. Samples depict mainly Ti, O and Si components but also carbon (C) and fluorine (F) contaminations. The presence of carbon in the sample could be explained by contamination during MACE and ALD processes. The presence of fluorine was detected only on the surface of as-prepared PSi and PSi/TiO_2 nanocomposite (100 ALD cycles) with a weak signal at 689.6 eV corresponding to F 1s electron. This peak was attributed to C—F or Si—F bonds which could be formed during MACE [30].

Using CasaXPS software, the elemental ratio of oxygen to titanium (O/Ti) was determined. In order to calculate the elemental ratio, we used only the peak areas corresponding to the Ti—O contributions within the O1s and Ti 2p core levels. The obtained values were 2.15, 2.23 and 2.22 for Si/TiO_2 nanocomposites, deposited by 100, 150 and 200 cycles, respectively. The higher values of the O/Ti ratio could be explained by increasing the concentration of the oxygen vacancies in TiO_2.

The main peak of the O ($KL_{23}L_{23}$) Auger series occurs at kinetic energy of 506.4 eV for PSi and at about 511 eV for PSi/TiO_2 nanocomposites. By using the values of O 1s binding energy and O (KL_{23} L_{23}) kinetic energy, we calculated the Auger parameter as defined by Wagner [31]. As was shown in our previous work, the phase, the stoichiometry and the crystallinity of surfaces could be determined using Auger parameter [12]. Our measurements lead to a value of 1039.8 eV for PSi and 1042.1 eV for PSi/TiO_2 nanocomposites corresponding to SiO_2 and TiO_2, respectively [32,33].

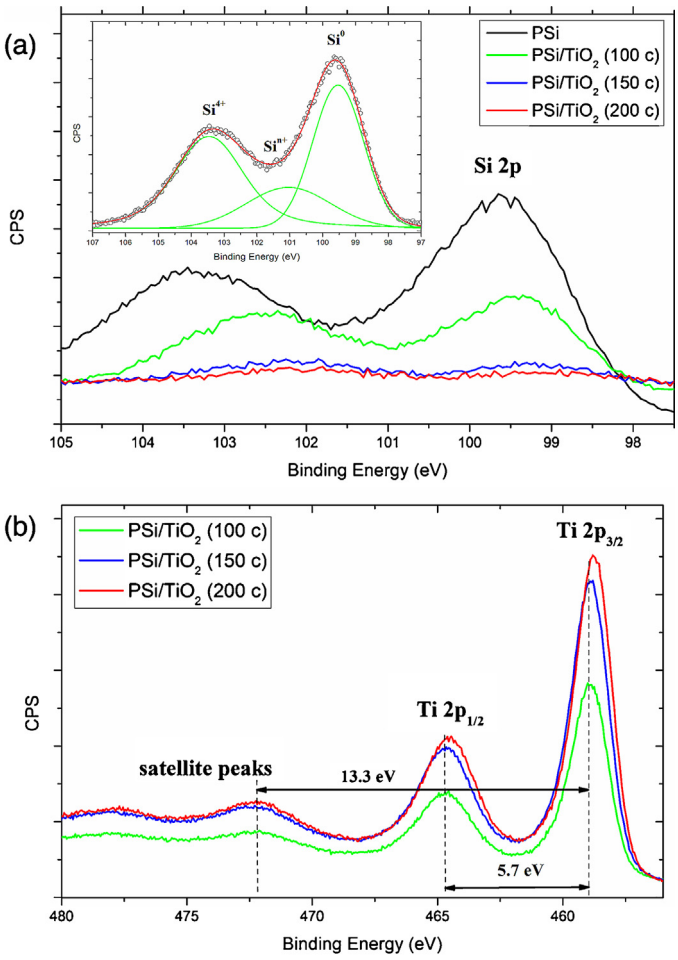

Fig. 5. The XPS spectra of Si 2p (a) and Ti 2p (b) with different number of ALD cycles. Inset of (a) shows the deconvolution of Si 2p.

3.3.2. XPS core-level spectra

The detailed spectra of Si 2p and Ti 2p core levels are shown in Fig. 5. The analysis of XPS spectra (Fig. 5a) shows that on the surface of the PSi there are silicon atoms in three states: neutral atoms (Si^0) with Si 2p binding energy of 99.5 ± 0.2 eV, charged silicon atoms (Si^{4+}) with a binding energy of 103.4 ± 0.2 eV characteristic of Si—O bonds and silicon atoms in the intermediate state (Si^{n+}) with a binding energy of about 101 eV [34,35]. The position of the silicon peaks shifts to lower binding energy after the ALD processes. The decreasing binding energy of the surface Si peak implies that the interfacial Si in SiO_2 formed during ALD has a lower binding energy than that of the original SiO_2.

Fig. 4b shows the core level of the Ti 2p spectrum of PSi/TiO_2 nanocomposites. The core level binding energies of Ti $2p_{3/2}$ and Ti $2p_{1/2}$ in the PSi/TiO_2 nanocomposite (100 ALD cycles) are 458.9 ± 0.2 eV and 464.6 ± 0.2 eV, respectively. By increasing the amount of ALD cycles, the peak positions of Ti $2p_{3/2}$ and $2p_{1/2}$ are found to be shifted toward a lower binding energy. However, the difference of 5.7 eV in all samples indicates the presence of the normal state of Ti^{4+} in the TiO_2 [36]. It might be explained by the

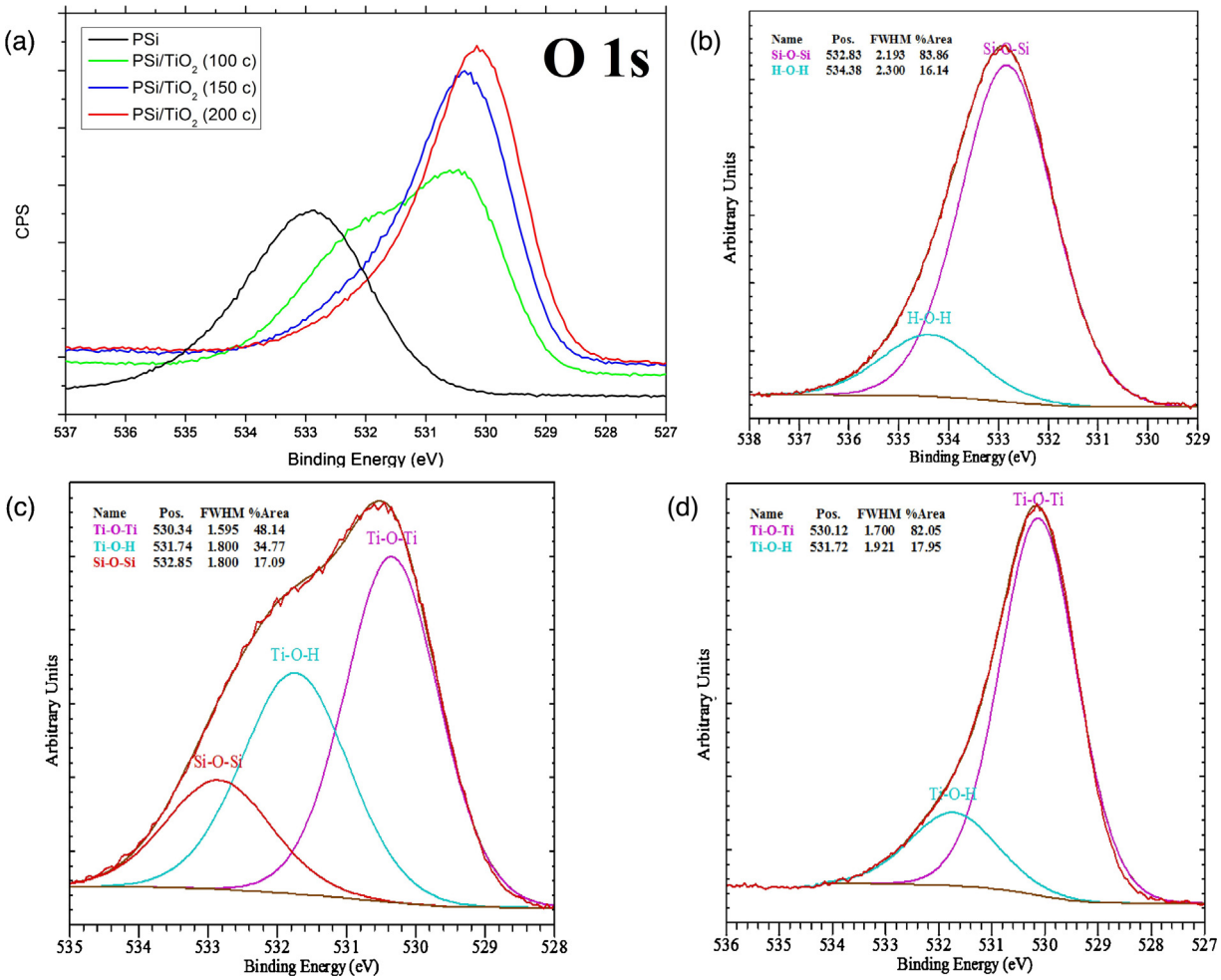

Fig. 6. (a) High resolution XPS core level spectra of O 1s, deconvoluted O 1s XPS line for (b) PSi, (c) PSi/TiO_2 (100 ALD cycles), (d) PSi/TiO_2 (200 ALD cycles).

interactions of Ti with oxygen vacancies [37]. As oxygen is a highly electronegative element, it withdraws the electron density from Ti. As a result, the binding energy of Ti in PSi/TiO_2 nanocomposites increases with increasing of the oxygen vacancies concentration [38].

Few peaks corresponding to the plasmon losses could be noticed in the Fig. 5b [39]. As can be seen in Fig. 5b, the satellite peak is observed at approximately 472.2 ± 0.2 eV, corresponding to surface plasmon energy E_p = 472.2 eV − $E_{Ti\,2p}$ = 13.3 eV which is characteristic of TiO_2 [39].

It is believed that several factors will affect the Si 2p and Ti 2p core levels shifting: the initial position of the Fermi level within the band gap, Schottky barrier formation, the surface band bending and the chemical effects. A consensus exists among the researches as to the behavior of the Si 2p and Ti 2p peaks and the core level shifting is mainly explained by the formation of Si—O—Ti bonds at the interface between SiO_2 and TiO_2 [40–42]. Because Si is more electronegative than Ti, the Si^{4+} binding energy should decrease as Ti is added to the Si—O bonds during deposition of TiO_2. On the other hand, the Ti^{4+} binding energy decreases as the TiO_2 becomes more bulklike with increasing the number of ALD cycles. As a result, the measured binding energies of both Si and Ti decrease with increasing the number of ALD cycles due to the change in electron screening of the core levels. Thus, the shift of the Si 2p and Ti 2p peaks observed after deposition indicates an interaction between Si and Ti at the interface through a Si—O—Ti bond [40–42].

Core level O 1s spectra for the PSi and PSi/TiO_2 nanocomposites are shown in Fig. 6. The spectrum for the as-prepared PSi has an asymmetric tail at higher energy. This peak was deconvoluted into two components at 532.8 ± 0.2 eV and 534.4 ± 0.2 eV. The main peak at 532.8 ± 0.2 eV is attributed to the oxygen (O^{2-}) which is chemically bonded to silicon, i.e., dioxide silicon [32,34]. The higher energy component of O 1s (534.4 ± 0.2 eV) should be due to adsorbed water [43].

The O 1s peak at 531.5 eV for the PSi/TiO_2 nanocomposite after 100 ALD cycles is relatively broad and asymmetric as it is associated with different types of bonds (Fig. 6b). Three distinct components, the peak locating at 530.4 ± 0.2 eV originated from Ti—O—Ti bonds, the other peak 532.8 ± 0.2 eV associated with Si—O—Si bonds [34,35], were revealed after deconvolution. The peak at 531.7 ± 0.2 eV could be related to Ti—O—H hydroxyl groups appeared due to H_2O in ALD [36–38]. However, it could also be associated with Si—O—Ti bonds at the interface between SiO_2 and TiO_2 [36–38].

The broad peak for the PSi/TiO_2 nanocomposite after 200 ALD cycles can be deconvoluted into two peaks centered at 530.1 ± 0.2 eV and 531.7 ± 0.2 eV. The peak at 531.7 ± 0.2 eV is attributed to Ti—O—H bonds, which should be located at about 1.6 eV higher binding energy corresponding to the O 1s of TiO_2 [36–38].

3.3.3. *Valence band spectra*

In order to investigate the modification of PSi/TiO_2 nanocomposites electronic structure the valence band spectra were measured and analyzed (Fig. 7). Fig. 7 shows the experimental and deconvoluted valence band spectra of PSi/TiO_2 nanocomposites.

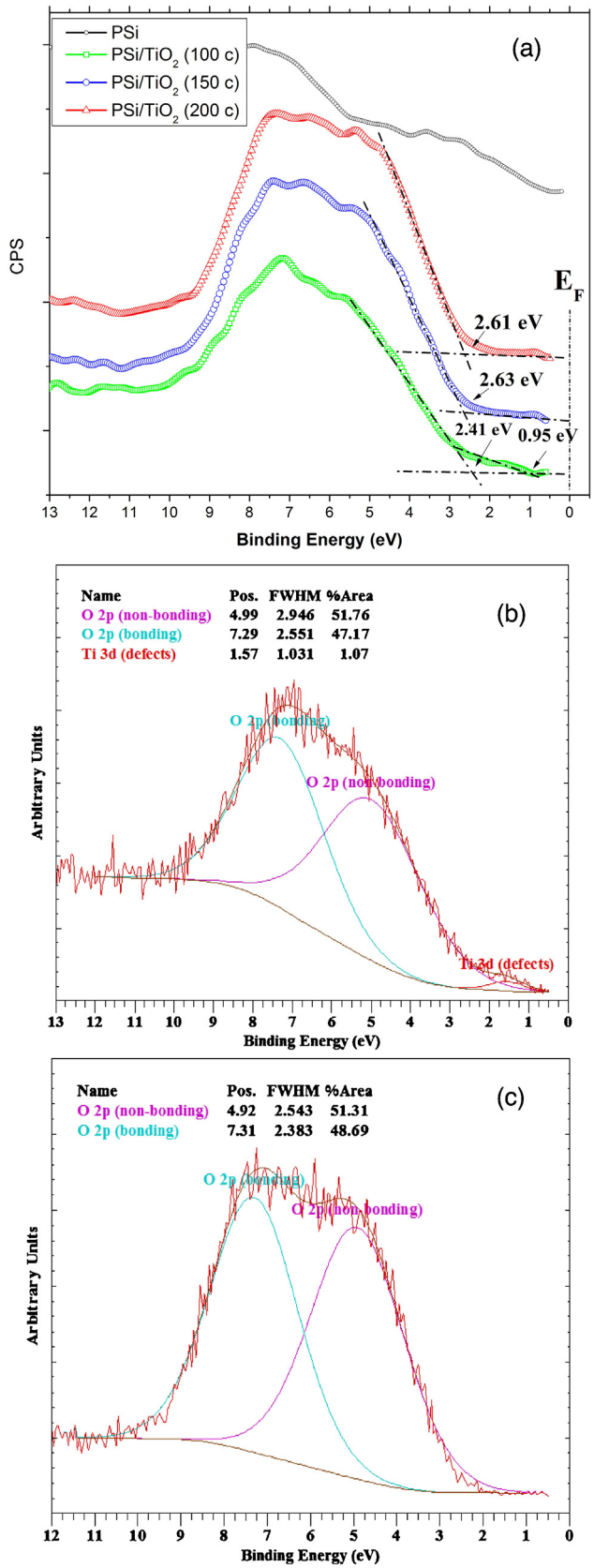

Fig. 7. (a) Valence band spectra plotted for all the samples; deconvoluted valence band spectra of PSi/TiO_2 nanocomposites for (b) 100 and (c) 200 ALD cycles.

The valence band maximum (VBM) relative to the Fermi level was determined using standard approach as described elsewhere [44]. The VBM of PSi/TiO_2 nanocomposites for 150 and 200 ALD cycles were observed at 2.63 eV and 2.61 eV below the E_F, respectively. While the VBM of the PSi/TiO_2 nanocomposite with 100 ALD cycles shows a small shift to 2.41 eV. Such shifting in the VBM has been related to the band gap variation or defect band formation in the forbidden zone of the material. According to our previous studies, the band gap values were 3.45, 3.3, and 3.25 for TiO_2 nanolayers deposited by 100, 150, and 200 cycles, respectively [14]. We assume that this shift is a cumulative effect of the band gap variation and the formation of impurity/defect states in the band gap of TiO_2, most probably corresponding to oxygen vacancies and surface hydroxyl groups on TiO_2 [14,45]. The valence band peak for the PSi/TiO_2 nanocomposite (200 ALD cycles) was deconvoluted into two components (Fig. 7c). Deconvoluted peaks are located at about 5 eV and 7.3 eV and corresponding to O 2p non-bonding orbitals (π – orbital) and O 2p – Ti 3d hybridized states (bonding σ – orbital), respectively [46]. Further deconvolution of the PSi/TiO_2 nanocomposite (100 ALD cycles) revealed three distinct components located at about 1.5 eV, 5 eV and 7.3 eV, (Fig. 7b). Peaks located at about 5 eV and 7.3 eV correspond to the same oxygen components as in previous sample. The peak centered at about 1.5 eV can be attributed to Ti 3d defect band. The VBM for this defect band is 0.95 eV (Fig. 7a). According to many authors, we can associate these states with Ti^{3+} defects on the surface [14,47,48]. Ti^{3+} defects are considered to be an important reactive agent for many processes occurring on the TiO_2 surface [49]. The photogenerated electrons can be trapped in Ti^{3+}, thereby decreasing the recombination rate of charge carriers. These point defects also play a crucial role in photocatalytic processes [50] and affect the hydrophilic property of the surface [51]. Thus, the unique combination of PSi and TiO_2 properties in the nanocomposite open new possibilities for various applications of these structures, where it is important to tune their physical properties by the morphology.

4. Conclusions

In this work, we have studied the structural and electronic properties of PSi/TiO_2 nanocomposites fabricated by ALD and MACE by means of electron microscopy, energy dispersive X-ray spectroscopy, Raman spectroscopy and X-ray photoelectron spectroscopy. The chemical composition and morphology of PSi/TiO_2 nanocomposites and initial PSi were established. It was determined that ALD TiO_2 infiltrates and coats the pores conformally forming nanocrystals of anatase inside the PSi matrix. It was shown that the electronic structure of PSi/TiO_2 nanocomposites is modified. Ti^{3+} defects states of PSi/TiO_2 nanocomposites were determined using XPS valence band analysis. Finally, it was suggested that combining the large effective surface area of TiO_2/PSi nanocomposites with the fast charge carrier separation allows one to improve the performance of biosensors, photocatalysts and other optoelectronic devices.

Acknowledgements

Financial support from the National Centre for Research and Development under research grant “Nanomaterials and their application to biomedicine”, contract number PBS1/A9/13/2012 is gratefully acknowledged.

References

[1] V.M. Arakelyan, V.E. Galstyan, K.S. Martirosyan, G.E. Shahnazaryan, V.M. Aroutiounian, P.G. Soukiassian, Hydrogen sensitive gas sensor based on porous silicon/TiO_{2-x} structure, Physica E 38 (2007) 219–221.

[2] V.V. Bolotov, P.M. Korusenko, S.N. Nesov, S.N. Povoroznyuk, V.E. Roslikov, E.A. Kurdyukova, Y.A. Steńkin, R.V. Shelyagin, E.V. Knyazev, V.E. Kan, I.V. Ponomareva, Nanocomposite por-Si/SnO_x layers formation for gas microsensors, Mater. Sci. Eng. B 177 (2012) 1–7.

[3] Dali Yan, Ming Hu, Shenyu Li, Jiran Liang, Yaqiao Wu, Shuangyun Ma, Electrochemical deposition of ZnO nanostructures onto porous silicon and their enhanced gas sensing to NO_2 at room temperature, Electrochim. Acta 115 (2014) 297–305.

[4] J. Li, M.J. Sailor, Synthesis and characterization of a stable, label-free optical biosensor fromTiO_2-coated porous silicon, Biosens. Bioelectron. 55 (2014) 372–378.

[5] H.S. Al-Salman, M.J. Abdullahc, Preparation of ZnO nanostructures by RF-magnetron sputtering on thermally oxidized porous silicon substrate for VOC sensing application, Measurement 59 (2015) 248–257.

[6] Qingping Wu, Danzhen Li, Zhixin Chen, Xianzhi Fu, New synthesis of a porous Si/TiO_2 photocatalyst: testing its efficiency and stability under visible light irradiation, Photochem. Photobiol. Sci. 5 (2006) 653–655.

[7] Y.S. Sakhare, S.V. Bhoraskar, V.L. Mathe, A.U. Ubale, Electric field assisted enhanced photo catalytic activities of immobilized nano TiO_2 on porous silicon, Mater. Res. Bull. 59 (2014) 205–213.

[8] Jian Shi, Xudong Wang, Hierarchical TiO_2–Si nanowire architecture with photoelectrochemical activity under visible light illumination, Energy Environ. Sci. 5 (2012) 7918–7922.

[9] A.M. Suhail, S. Salman, F.E. Naoum, H.A. Thjeel, Q.G. Al Zaidi, ZnO/porous-silicon photovoltaic UV detector, J. Electron Devices 13 (2012) 900–909.

[10] K.A. Salman, K. Omar, Z. Hassan, Effective conversion efficiency enhancement of solar cell using ZnO/PS antireflection coating layers, Solar Energy 86 (2012) 541–547.

[11] L. Martínez, O. Oscar, Y. Kumar, V. Agarwal, ZnO-porous silicon nanocomposite for possible memristive device fabrication, Nanoscale Res. Lett. 9 (2014) 437.

[12] I. Iatsunskyi, M. Kempinski, M. Jancelewicz, K. Załeski, S. Jurga, V. Smyntyna, Structural and XPS characterization of ALD Al_2O_3 coated porous silicon, Vacuum 113 (2015) 52–58.

[13] M. Rajabi, R.S. Dariani, A. Iraji Zad, UV photodetection of laterally connected ZnO rods grown on porous silicon substrate, Sens. Actuators A 180 (2012) 11–14.

[14] I. Iatsunskyi, M. Pavlenko, R. Viter, M. Jancelewicz, G. Nowaczyk, I. Baleviciute, K. Załęski, S. Jurga, A. Ramanavicius, V. Smyntyna, Tailoring the structural, optical, and photoluminescence properties of porous silicon/TiO_2 nanostructures, J. Phys. Chem. C 119 (2015) 7164–7171.

[15] Fuchao Yang, Shuyi Ma, Xiaolei Zhang, Meng Zhang, Faming Li, Jing Liu, Qiang Zhao, Blue–green and red luminescence from ZnO/porous silicon and ZnO:Cu/porous silicon nanocomposite films, Superlattices Microstruct. 52 (2012) 210–220.

[16] Wei Qin, Songtao Lu, Xiaohong Wu, Song Wang, Dye-sensitized Solar cell based on N-doped TiO_2 electrodes prepared on titanium, Int. J. Electrochem. Sci. 8 (2013) 7984–7990.

[17] A. Sedghi, H.N. Miankushki, Influence of TiO_2 electrode properties on performance of dye sensitized solar cells, Int. J. Electrochem. Sci. 7 (2012) 12078–12089.

[18] T. Touam, L. Znaidi, D. Vrel, I. Ninova-Kuznetsova, O. Brinza, A. Fischer, A. Boudrioua, Low loss sol–gel TiO_2 thin films for waveguiding applications, Coatings 3 (2013) 49–58.

[19] K.H. Leong, P. Monash, S. Ibrahim, P. Saravanan, Solar photocatalytic activity of anatase TiO_2 nanocrystals synthesized by non-hydrolytic sol–gel method, Solar Energy 101 (2014) 321–332.

[20] Bocheng Qiu, Mingyang Xing, Jinlong Zhang, Mesoporous TiO_2 nanocrystals grown in situ on graphene aerogels for high photocatalysis and lithium-ion batteries, J. Am. Chem. Soc. 136 (2014) 5852–5855.

[21] T. Nam, J.M. Kim, M.K. Kim, H. Kim, Low-temperature atomic layer deposition of TiO_2, Al_2O_3, and ZnO thin films, J. Korean Phys. Soc. 59 (2011) 452–457.

[22] Z. Huang, N. Geyer, P. Werner, J. de Boor, U. Gösele, Metal-assisted chemical etching of silicon: a review, Adv. Mater. 23 (2011) 285–308.

[23] D. Wang, Y. Yan, P. Schaaf, ZnO/porous-Si and TiO_2/porous-Si nanocomposite nanopillars, Vac. Sci. Technol. A 33 (2015) 01A102.

[24] H. Tanino, A. Kuprin, H. Deai, Raman study of free-standing porous silicon, Phys. Rev. B 53 (4) (1996) 1937–1947.

[25] I. Iatsunskyi, S. Jurga, V. Smyntyna, M. Pavlenko, V. Myndrul, A. Zaleska, Raman spectroscopy of nanostructured silicon fabricated by metal-assisted chemical etching, Proc. SPIE – Int. Soc. Opt. Eng. 9132 (2014) (art. no. 913217).

[26] A. Niilisk, M. Moppel, M. Pears, I. Sildos, T. Jantson, T. Avarmaa, R. Jaaniso, J. Aarik, Structural study of TiO_2 thin films by micro-Raman spectroscopy, Cent. Eur. J. Phys. 4 (2006) 105.

[27] Ke-Rong Zhu, Ming-Sheng Zhang, Qiang Chen, Zhen Yin, Size and phonon-confinement effects on low-frequency Raman mode of anatase TiO_2 nanocrystal, Phys. Lett. A 340 (2005) 220–227.

[28] D. Bersani, P.P. Lottici, X.-Z. Ding, Phonon confinement effects in the Raman scattering by TiO_2 nanocrystals, Appl. Phys. Lett. 72 (1998) 73.

[29] W.F. Zhang, Y.L. He, M.S. Zhang, Z. Yin, Q. Chen, Raman scattering study on anatase TiO_2 nanocrystals, J. Phys. D: Appl. Phys. 33 (2000) 912–916.

[30] F.-Y. Zhanga, S.G. Advani, A.K. Prasada, M.E. Boggs, S.P. Sullivanc, T.P. Beebe Jr., Quantitative characterization of catalyst layer degradation in PEM fuel cells by X-ray photoelectron spectroscopy, Electrochim. Acta 54 (2009) 4025–4030.

[31] G. Moretti, Auger parameter and Wagner plot in the characterization of chemical states by X-ray photoelectron spectroscopy: a review, J. Electron Spectrosc. Relat. Phenom. 95 (1998) 95–144.

[32] C.D. Wagner, D.E. Passoja, H.F. Hillery, T.G. Kinisky, H.A. Six, W.T. Jansen, J.A. Taylor, Auger and photoelectron line energy relationships in aluminum–oxygen and silicon–oxygen compounds, J. Vac. Sci. Technol. 21 (1982) 933.

[33] C.D. Wagner, D.A. Zatko, R.H. Raymond, Use of the oxygen KLL Auger lines in identification of surface chemical states by electron spectroscopy for chemical analysis, Anal. Chem. 52 (1980) 1445.

[34] N. Koshizaki, H. Umehara, T. Oyama, XPS characterization and optical properties of Si/SiO_2, Si/Al_2O_3 and Si/MgO co-sputtered films, Thin Solid Films 325 (1998) 130–136.

[35] D.S. Jensen, S.S. Kanyal, N. Madaan, M.A. Vail, A.E. Dadson, M.H. Engelhard, M.R. Linford, Silicon (1 0 0)/SiO_2 by XPS, Surf. Sci. Spectra 20 (2013) 36.

[36] C. Rath, P. Mohanty, A.C. Pandey, N.C. Mishra, Oxygen vacancy induced structural phase transformation in TiO_2 nanoparticles, J. Phys. D: Appl. Phys. 42 (2009) 205101.

[37] S. Sharma, S. Chaudhary, S.C. Kashyap, S.K. Sharma, Room temperature ferromagnetism in Mn doped TiO_2 thin films: electronic structure and Raman investigations, J. Appl. Phys. 109 (2011) 083905.

[38] F. Dong, S. Guo, H. Wang, X. Li, Z. Wu, Enhancement of the visible light photocatalytic activity of C-doped TiO_2 nanomaterials prepared by a green synthetic approach, J. Phys. Chem. C 115 (2011) 13285–13292.

[39] M. Oku, H. Matsuta, K. Wagatsuma, Y. Waseda, S. Kohiki, Removal of inelastic scattering part from Ti 2p XPS spectrum of TiO_2 by deconvolution method using O 1s as response function, J. Electron Spectrosc. Relat. Phenom. 105 (1999) 211–218.

[40] J. Finster, D. Schulze, F. Bechstedt, A. Meisel, Interpretation of XPS core level shifts and structure of thin silicon oxide layers, Surf. Sci. 152/153 (1985) 1063–1070.

[41] N. Benito, C. Palacio, Growth of Ti–O–Si mixed oxides by reactive ion-beam mixing of Ti/Si interfaces, J. Phys. D: Appl. Phys. 47 (2014) 015308.

[42] R. Methaapanon, S.F. Bent, Comparative study of titanium dioxide atomic layer deposition on silicon dioxide and hydrogen-terminated silicon, J. Phys. Chem. C 114 (2010) 10498–10504.

[43] S. Yamamoto, H. Bluhm, K. Andersson, G. Ketteler, H. Ogasawara, M. Salmeron, A. Nilsson, In situ X-ray photoelectron spectroscopy studies of water on metals and oxides at ambient conditions, J. Phys.: Condens. Matter 20 (2008) 184025.

[44] M. Mansoob Khan, S.A. Ansari, D. Pradhan, M.O. Ansari, Do Hung Han, Jintae Lee, Moo Hwan Cho, Band gap engineered TiO_2 nanoparticles for visible light induced photoelectrochemical and photocatalytic studies, Mater. Chem. A 2 (2014) 637–644.

[45] Gongming Wang, Hanyu Wang, Yichuan Ling, Yuechao Tang, Xunyu Yang, R.C. Fitzmorris, Changchun Wang, J.Z. Zhang, Yat Li, Hydrogen-treated TiO_2 nanowire arrays for photoelectrochemical water splitting, Nano Lett. 11 (2011) 3026–3033.

[46] U. Diebold, The surface science of titanium dioxide, Surf. Sci. Rep. 48 (2003) 53–229.

[47] A.G. Thomas, W.R. Flavell, A.R. Kumarasinghe, A.K. Mallick, D. Tsoutsou, G.C. Smith, R. Stockbauer, S. Patel, M. Grätzel, R. Hengerer, Resonant photoemission of anatase TiO_2 (1 0 1) and (0 0 1) single crystals, Phys. Rev. B 67 (2003) 035110.

[48] K. Bapna, D.M. Phase, R.J. Choudhary, Study of valence band structure of Fe doped anatase TiO_2 thin films, J. Appl. Phys. 110 (2011) 043910.

[49] H.B. Kim, D.W. Park, J.P. Jeun, S.H. Oh, Y.C. Nho, P.H. Kang, Effects of electron beam irradiation on the photoelectrochemical properties of TiO_2 film for DSSCs, Radiat. Phys. Chem. 81 (2012) 954–957.

[50] A. Sirisuk, E. Klansorn, P. Praserthdam, Effects of reaction medium and crystallite size on Ti^{3+} surface defects in titanium dioxide nanoparticles prepared by solvothermal method, Catal. Commun. 9 (2008) 1810–1814.

[51] N. Sakai, A. Fujishima, T. Watanabe, K. Hashimoto, Quantitative evaluation of the photoinduced hydrophilic conversion properties of TiO_2 thin film surfaces by the reciprocal of contact angle, J. Phys. Chem. B 107 (2003) 1028–1035.